Supplement of The Cryosphere, 19, 1955–1971, 2025
https://doi.org/10.5194/tc-19-1955-2025-supplement


The Cryosphere

*Supplement of*

# Anisotropic scattering in radio-echo sounding: insights from northeast Greenland

**Tamara Annina Gerber et al.**

*Correspondence to:* Tamara Annina Gerber (tamara.gerber@unil.ch)

# S1 Simulating azimuthal response with ice-core COF

We use the matrix-based layer model for two-way radar wave propagation by Fujita et al. (2006) to simulate the theoretical azimuthal response at EastGRIP. For nadir-propagating waves, as is the case here, a $2 \times 2$ matrix model is sufficient, but $4 \times 4$ matrices are needed otherwise (Rathmann et al., 2022).

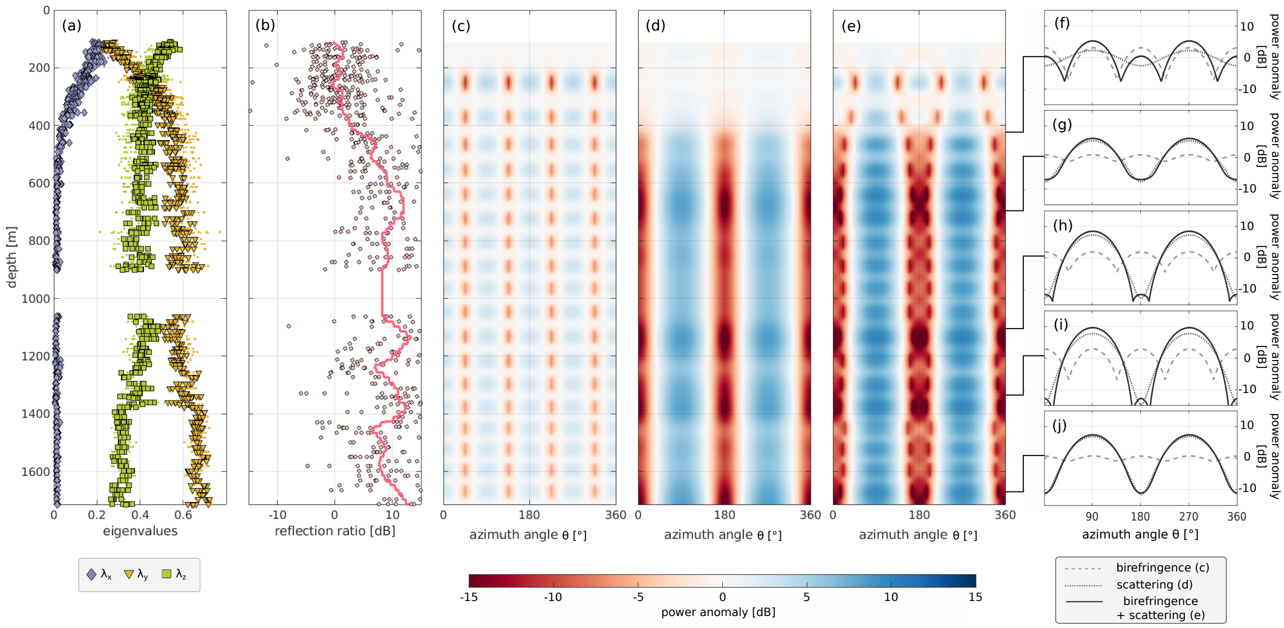


Fig. S1: Simulated radar response with 330 MHz center frequency and ice-core derived scattering and birefringence properties: Panel (**a**) shows the EastGRIP COF eigenvalues from Zeising et al. (2023), where purple correspond to $\lambda_1$, orange to $\lambda_2$ and green to $\lambda_3$. $\lambda_x$ is approximately parallel to surface flow direction at EastGRIP. Dots of the corresponding colors are the pure eigenvalues, while squares, triangles and diamonds are the eigenvalues weighted to grain size. Panel (**b)** shows the reflection ratio derived form Eq. (S4) (dots) and smoothed over 50 m (line), assuming that the eigenvalue variation with depth is its sole contribution. Panels (**c–e**) show the co-polarized power anomalies ($\mathrm{dP_{HH}}$) of the radar response from birefringence, COF-induced anisotropic scattering and the combined effect simulated with the matrix-based model by Fujita et al. (2006). y-axes correspond to depth along the ice core and x-axes indicate polarization azimuth with $\theta = 0$ corresponding to model $x$-direction (i.e. $\lambda_x$, assumed to be flow-parallel). Panels (**f–j**) show the power anomalies as a function of azimuth for selected depths, indicated by lines connected to panel (e).

Analogous to Fujita et al. (2006), we simulate the individual response of birefringence and anisotropic scattering, as well as the combined effect. For cases with birefringence we use the EastGRIP crystal orientation fabric (COF) record by Zeising et al. (2023) to calculate the components of the transmission matrix **T**. The COF has been analyzed in discrete samples at intervals of 10–15 m using an automated fabric analyzer and is statistically described in terms of eigenvalues, with its two horizontal components $\lambda_x$ and $\lambda_y$, and $\lambda_z$ being vertical (Fig. S1a). We define the model $x$-direction as being parallel to the ice-flow direction at EastGRIP, and assume $\lambda_x$ is flow-parallel following observations by Westhoff et al. (2021). The directional relative permittivity profiles $\varepsilon'_x$ and $\varepsilon'_y$ are calculated from the two horizontal grain-size weighted eigenvalues $\lambda_x$ and $\lambda_y$

$$\varepsilon'_{x,y}(z) = \varepsilon'_\perp + \Delta\varepsilon' \lambda_{x,y}, \tag{S1}$$

where $\varepsilon'_\perp = 3.15$ is the relative permittivity component perpendicular to the c-axis, and $\Delta\varepsilon'$ is assumed to be 0.034 (Matsuoka et al., 1997). We use a model with a regular layer thickness of 1 m, ranging from 111 m to 1700 m depth and interpolated the COF dataset linearly between measurements to match the vertical resolution of the model.

Our modeling assumes that the sole origin for anisotropic scattering is COF variations with depth, so we can estimate the components of the scattering matrix $\mathbf{S}_i$ from the impedance-derived scattering coefficient following Fujita et al. (2000)

$$S_{x,i} = \frac{Z_{x,i+1} - Z_{x,i}}{Z_{x,i+1} + Z_{x,i}} \text{ and } S_{y,i} = \frac{Z_{y,i+1} - Z_{y,i}}{Z_{y,i+1} + Z_{y,i}} \tag{S2}$$

with impedance in layer $i$ defined as

$$Z_{x,i} = \frac{\mathrm{j}\mu_0\omega}{k_{x,i}} \text{ and } Z_{y,i} = \frac{\mathrm{j}\mu_0\omega}{k_{y,i}}. \tag{S3}$$

The anisotropic reflection ratio in dB is then

$$r_i = 10\log_{10}\left(\frac{S_{y,i}}{S_{x,i}}\right). \tag{S4}$$

We smoothed the scattering coefficients with a moving average filter with window length of 50 m. The transmission and reflection matrices were kept isotropic for the pure scattering ($T_x = T_y$) and pure birefringence ($S_x = S_y$) scenarios, respectively.

The co- and cross-polarized power anomalies $\mathrm{dP_{HH}}$ and $\mathrm{dP_{HV}}$ are defined as (Dall, 2010; Jordan et al., 2019; Ershadi et al., 2022)

$$\mathrm{dP}_{xx}(\theta, z) = 20\log_{10}\left(\frac{|M_\mathrm{P}^{xx}(\theta, z)|}{\frac{1}{n}\sum_{b=1}^{n}|M_\mathrm{P}^{xx}(\theta_b, z)|}\right), \tag{S5}$$

where $M_\mathrm{P}^{xx}$ corresponds to the HH and HV component of the propagation matrix

$$\mathbf{M}_\mathrm{P} = \begin{pmatrix} M_\mathrm{P}^\mathrm{HH} & M_\mathrm{P}^\mathrm{HV} \\ M_\mathrm{P}^\mathrm{HV} & M_\mathrm{P}^\mathrm{VV} \end{pmatrix}, \tag{S6}$$

and $n$ is the number of angular increments of azimuth $\theta$ (Ershadi et al., 2022). Here, we introduce the term *propagation matrix* for $\mathbf{M}_\mathrm{P}$ instead of the *scattering matrix* used in the definition by Ershadi et al. (2022) in order to avoid confusion with the scattering matrix used above in the sense of the definition by Fujita et al. (2006). The propagation matrix combines the propagation in the subsurface:

$$\mathbf{E}_\mathrm{R} = \mathbf{M}_\mathrm{P}\mathbf{E}_\mathrm{T}, \tag{S7}$$

where $\mathbf{E}_\mathrm{R}$ and $\mathbf{E}_\mathrm{T}$ are the received and transmitted electrical fields. The full form of the propagation matrix $\mathbf{E}_\mathbf{P}$ is

$$\mathbf{M}_\mathrm{P} = \frac{\exp(jk_0z)^2}{(4\pi z)^2} \times \prod_{i=1}^{N}[\mathbf{R}(\theta_{N+1-i})\mathbf{T}_{N+1-i}\mathbf{R}'(\theta_{N+1-i})] \times \mathbf{R}(\theta_i)\mathbf{S}_i\mathbf{R}'(\theta_i)\prod_{i=1}^{N}[\mathbf{R}(\theta_i)\mathbf{T}_i\mathbf{R}'(\theta_i)]. \tag{S8}$$

# S2 Comparison of model and RES

Here we compare the ice-core based model azimuthal response of both birefringence and anisotropic scattering (Fig. S1e), with observations from radio-echo sounding (RES) data near the ice-core drill site. The amplitude of the COF-derived reflection ratio in the model is nearly twice as high as that observed for anisotropic scattering in RES data. This discrepancy may stem from the low sampling rate of COF measurements, which might fail to capture eigenvalue variations that are smoother in reality. Consequently, the actual reflection ratio may be lower than suggested by the COF data. To account for this, we use a value of 0.5 $r$[dB] for comparison with the RES data. The full azimuthal response can be synthesized from single quad-polarized measurements (Ershadi et al., 2022) with

$$\mathbf{M}_\mathrm{P}(\theta + \gamma) = \mathbf{R}(\theta + \gamma)\mathbf{M}_\mathrm{P}(\theta)\mathbf{R}'(\theta + \gamma), \tag{S9}$$

where $\gamma$ is the angular offset between the initial radar orientation $\theta$ and the desired azimuth angle.

The complex co-polarized coherence for depth $n$ is defined as

$$C_{\mathrm{HHVV},n} = \frac{\sum_{b=n}^{n+N} M_{\mathrm{P},b}^{\mathrm{HH}} M_{\mathrm{P},b}^{*\mathrm{VV}}}{\sqrt{\sum_{b=n}^{n+N} |M_{\mathrm{P},b}^{\mathrm{HH}}|^2} \sqrt{\sum_{b=n}^{n+N} |M_{\mathrm{P},b}^{\mathrm{VV}}|^2}}, \tag{S10}$$

where $N$ is the number of depth bins used for averaging and $^*$ is the complex conjugate. Here, we average over a vertical depth of 50 m. The coherence phase difference then follows as

$$\phi_{\mathrm{HHVV}} = \arg(C_{\mathrm{HHVV}}), \tag{S11}$$

and the normalized gradient of $\phi_{\mathrm{HHVV}}$ is

$$\psi_{\mathrm{HHVV}} = \frac{2c_0\sqrt{\varepsilon'}}{4\pi f_c \Delta\varepsilon'} \frac{\mathrm{d}\phi_{\mathrm{HHVV}}}{\mathrm{d}z}. \tag{S12}$$

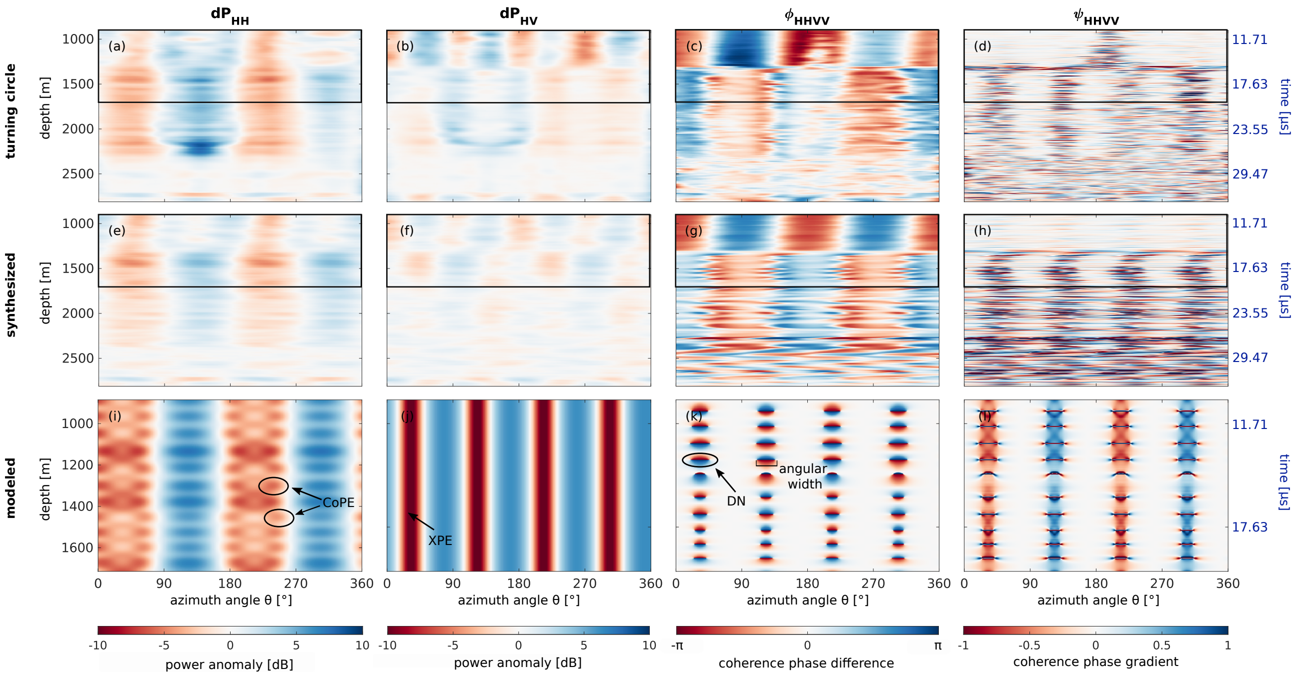


Fig. S2: From left to right, the figure shows co-polarized power anomaly ($\mathrm{dP_{HH}}$; panel (**a**), (**e**), (**i**)), cross-polarized power anomaly ($\mathrm{dP_{HV}}$; (**b**), (**f**), (**j**)), coherence phase difference ($\phi_{\mathrm{HHVV}}$; (**c**), (**g**), (**k**)), and the depth gradient of $\phi_{\mathrm{HHVV}}$ ($\psi_{\mathrm{HHVV}}$, (**d**), (**h**), (**l**)) versus polarization azimuth clockwise from True North. From top to bottom, the panels show the radar response from the circular radargram (**a**–**d**), synthesized from the quad-polarized measurements from the same radargram (**e**–**h**), and modeled with the COF record from the EastGRIP core (**i**–**l**). Notice the different depth range of the modeled result (indicated by the black frame in (**a**)–(**h**) due to restrictions from available COF data. Co-polarized power extinction (CoPE) nodes, cross-polarized power extinction (XPE), coherence phase dipole nodes (DN) and their angular width are exampled in (**i**–**k**).

Figure S2 shows the azimuthal power anomalies ($\mathrm{dP_{HH}}$, $\mathrm{dP_{HV}}$), the coherence phase difference ($\Phi_{\mathrm{HHVV}}$) and its depth gradient ($\psi_{\mathrm{HHVV}}$) for the turning circle (panel a–d), synthesized (panel e–h) and modeled (panel i–l) data, respectively, whereby the azimuth on the $x$-axes corresponds to clockwise angle from True North. The synthesized response was calculated from a single point at the beginning of the turning circle, where the driving direction was constant. This point was chosen to mitigate the impact of azimuthal discrepancies caused by the integration process, which smooths each polarization mode over a horizontal distance of approximately 3 m. The power anomalies and coherence phase difference/gradient of the turning circle and the synthesized response (panel a–h in Fig. S2) have been smoothed with a 2D Gaussian filter with standard deviation of 10 pixels.

The features in the turning circle and synthesized response match quite well, which gives confidence in using the synthesized response to evaluate azimuthal power fluctuations elsewhere, and shows that the radar system has sufficient radiometric calibration and phase synchronization across channels. The general pattern in the radar data consistently shows highest co-polarized return power at an azimuth of roughly 135–140° and 315–320°. However, in the modeled response, this pattern is slightly shifted with respect to the observed data by $\sim$10–15° and maximum co-polarized power appears at 125° and at 305°, respectively. The radar-derived amplitude of the $dP_{HH}$ power anomaly increases at a depth of $\sim$1400 m and is also slightly higher at $\sim$1700 m, both of which is also shown by the model. The latter additionally shows a higher $dP_{HH}$ at 1150 m depth which is not confirmed by radar observations. Instead, depths shallower than 1300 m in the radar data are characterized by lower amplitudes and a pattern dominated by 90° periodicity.

The observed and synthesized cross-polarized power anomalies ($dP_{HV}$, see panel b, f) show a notable azimuth shift of the XPE at 1250 m depth towards smaller azimuth angles which is not shown in the model. The underlying cause of this is presumably a rotation of COF eigenvectors not captured in the reconstructed orientation of the ice core (Zeising et al., 2023). However, the XPE azimuth below 1250 m is constant with depth and agrees well between the modeled and observed data for the depth span covered by the model, although here too, the azimuth between model and radar is shifted by approximately 10°.

The modeled coherence phase shows a large number of dipole nodes (DN) with an angular width of approximately 15–30° while individual nodes are hard to recognize in the turning circle and synthesized response, and angular widths are notably smaller. The phase–depth gradient can, in principle, be used as indication of eigenvector orientation, with negative gradients indicating the orientation of the smaller horizontal eigenvalue (Jordan et al., 2019; Ershadi et al., 2022). While this can be confirmed by the model, the phase gradient of the observed and synthesized data turn out to be too noisy to derive eigenvector orientations. However, the width of the zones with phase-gradient close to zero is similar between model and observations, indicating that the amount of anisotropic scattering between the two is comparable (Jordan et al., 2019). In the synthesized data, and partially also in the turning circle, the phase gradient above $\sim$1250 m depth is considerably smaller than below, which might indicate weaker horizontal anisotropy, but is not confirmed by the model.

## Supplementary Figures

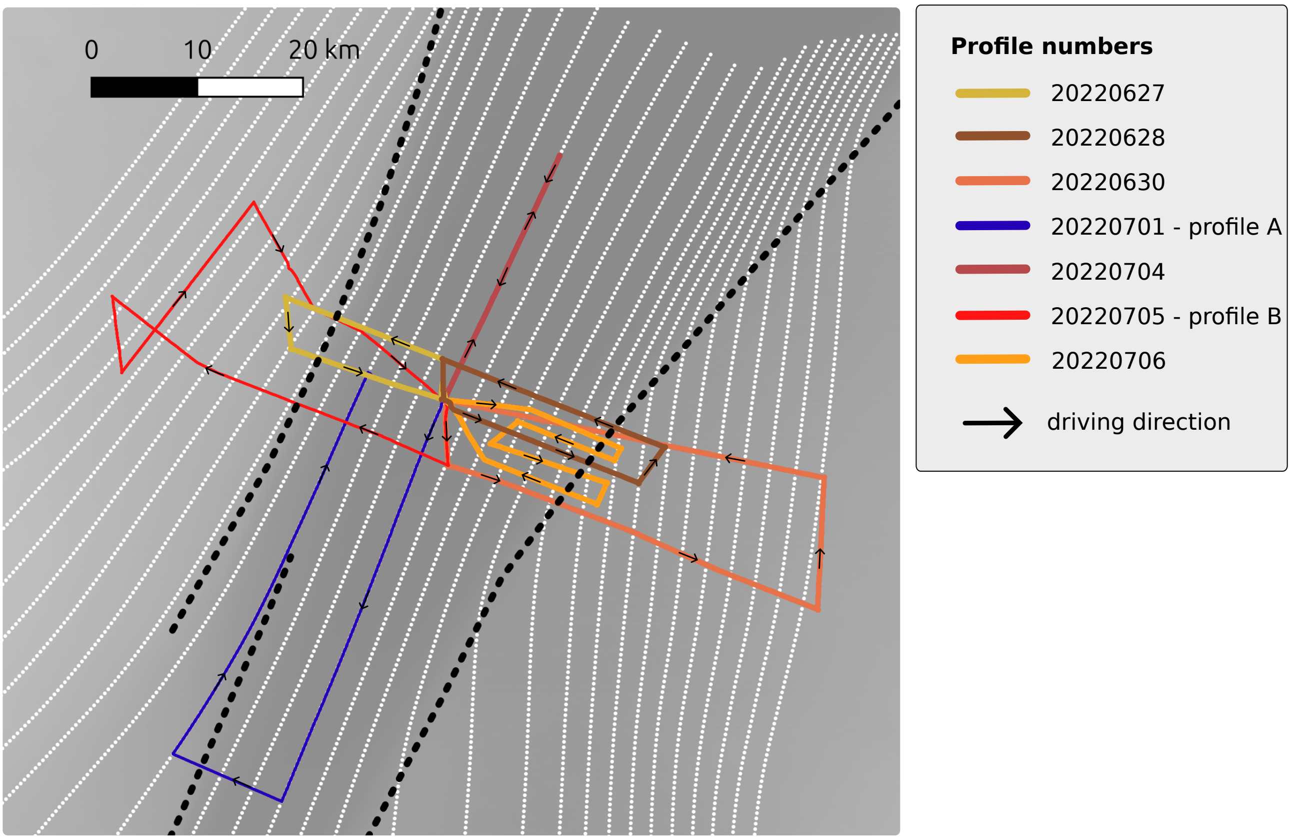


Fig. S3: Overview of profile names and driving directions. Profile '20220704' was measured double on the way back to camp upon turning at the downstream end.

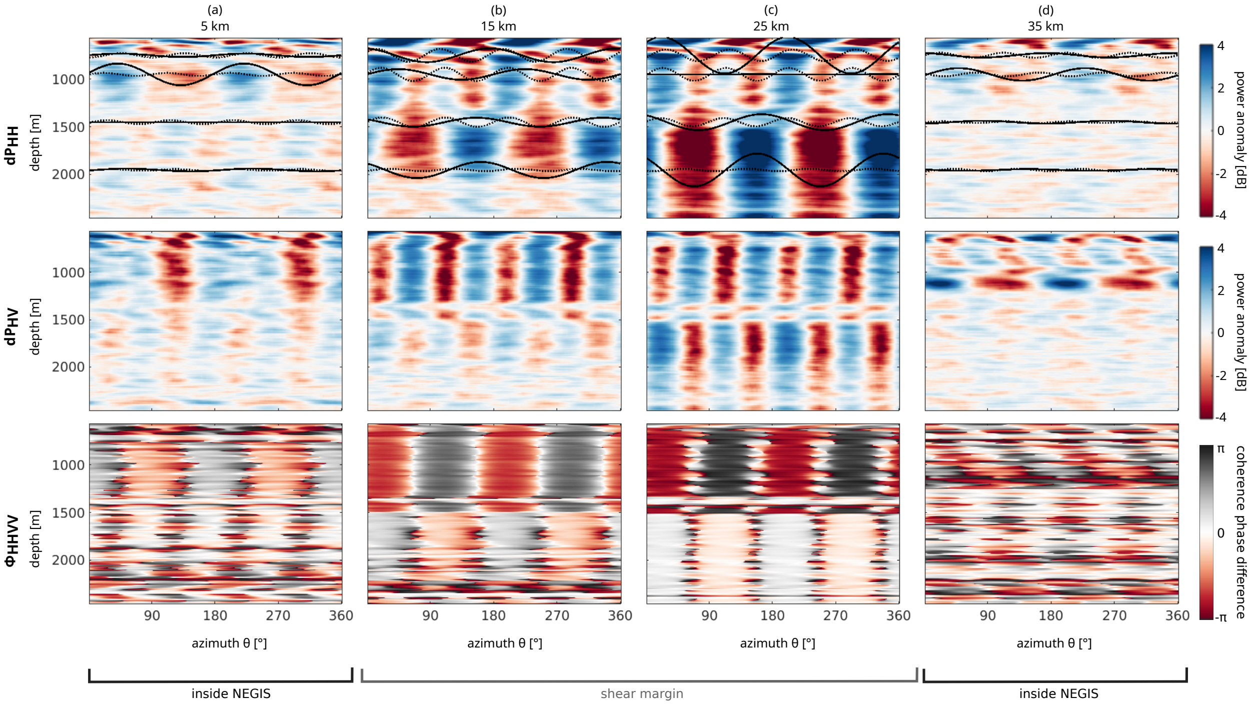


Fig. S4: Synthesized azimuthal radar response for profile '20220627': top panels show the co-polarized power anomaly $dP_{HH}$, middle panels show the cross-polarized power anomaly $dP_{HV}$, and bottom panels show the coherence phase difference $\phi_{HHVV}$.

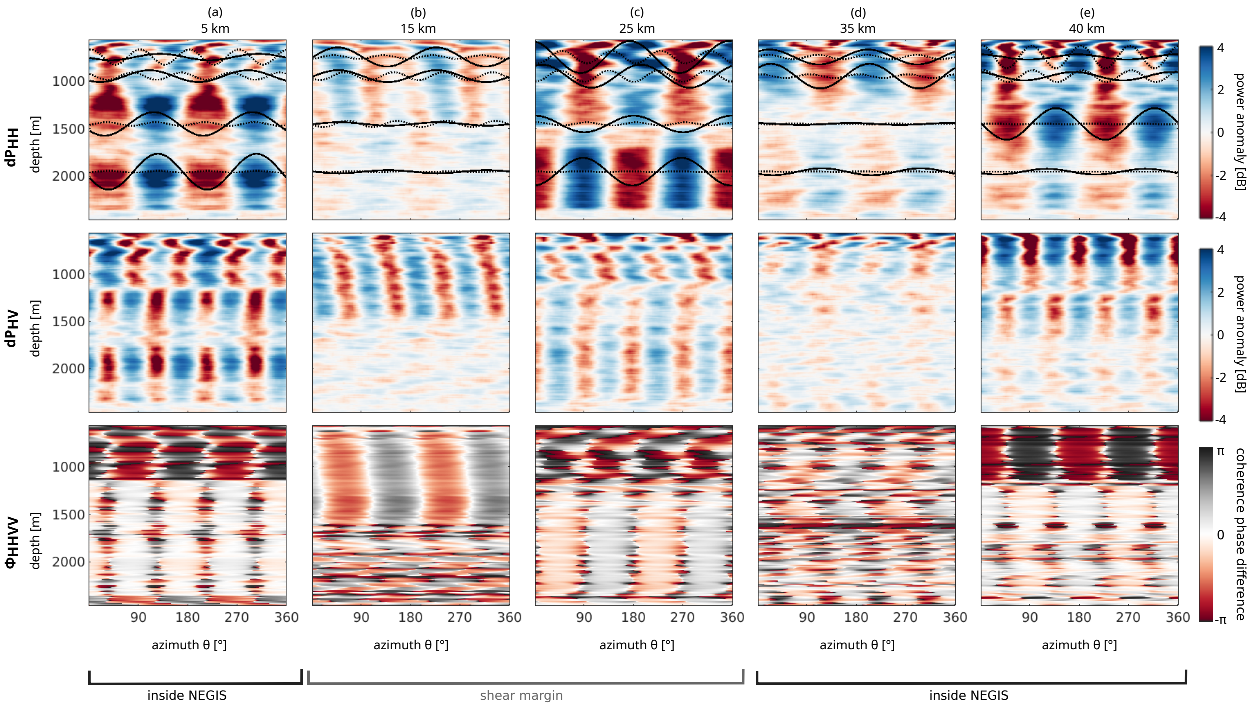


Fig. S5: Synthesized azimuthal radar response for profile '20220628': top panels show the co-polarized power anomaly $dP_{HH}$, middle panels show the cross-polarized power anomaly $dP_{HV}$, and bottom panels show the coherence phase difference $\phi_{HHVV}$.

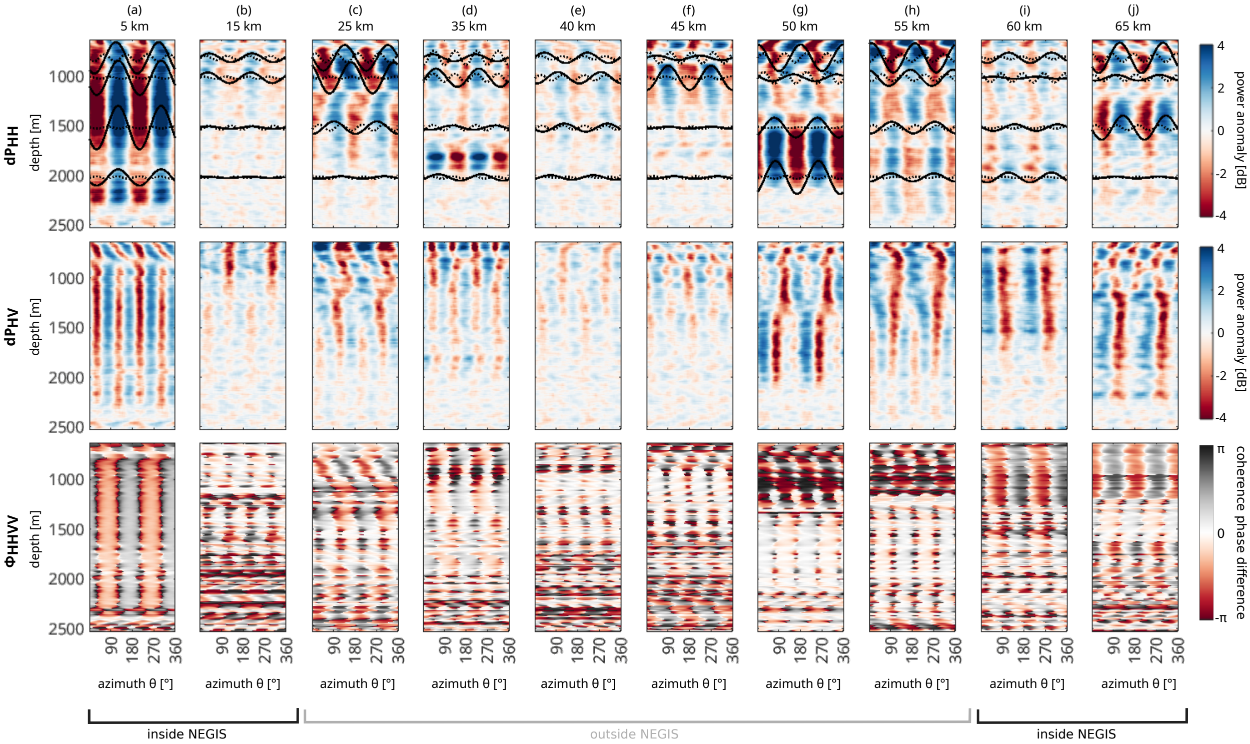


Fig. S6: Synthesized azimuthal radar response for profile '20220630': top panels show the co-polarized power anomaly $dP_{HH}$, middle panels show the cross-polarized power anomaly $dP_{HV}$, and bottom panels show the coherence phase difference $\phi_{HHVV}$.

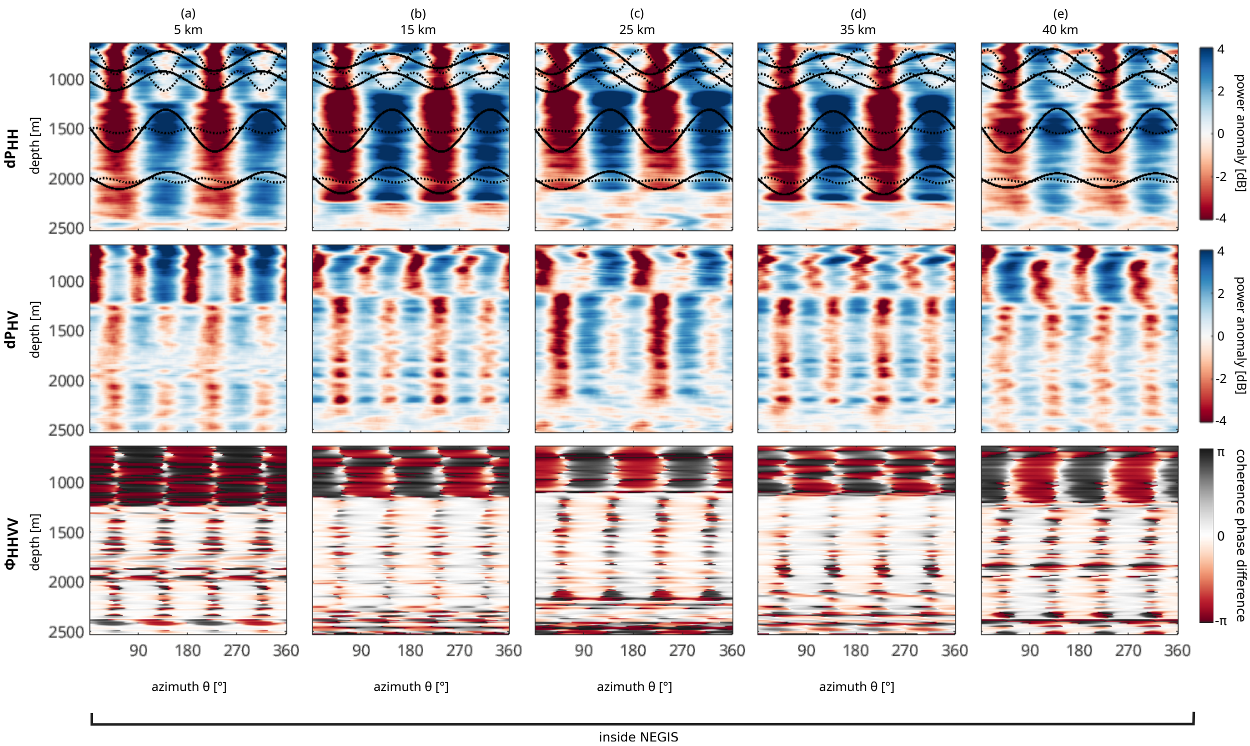


Fig. S7: Synthesized azimuthal radar response for profile '20220704': top panels show the co-polarized power anomaly $dP_{HH}$, middle panels show the cross-polarized power anomaly $dP_{HV}$, and bottom panels show the coherence phase difference $\phi_{HHVV}$.

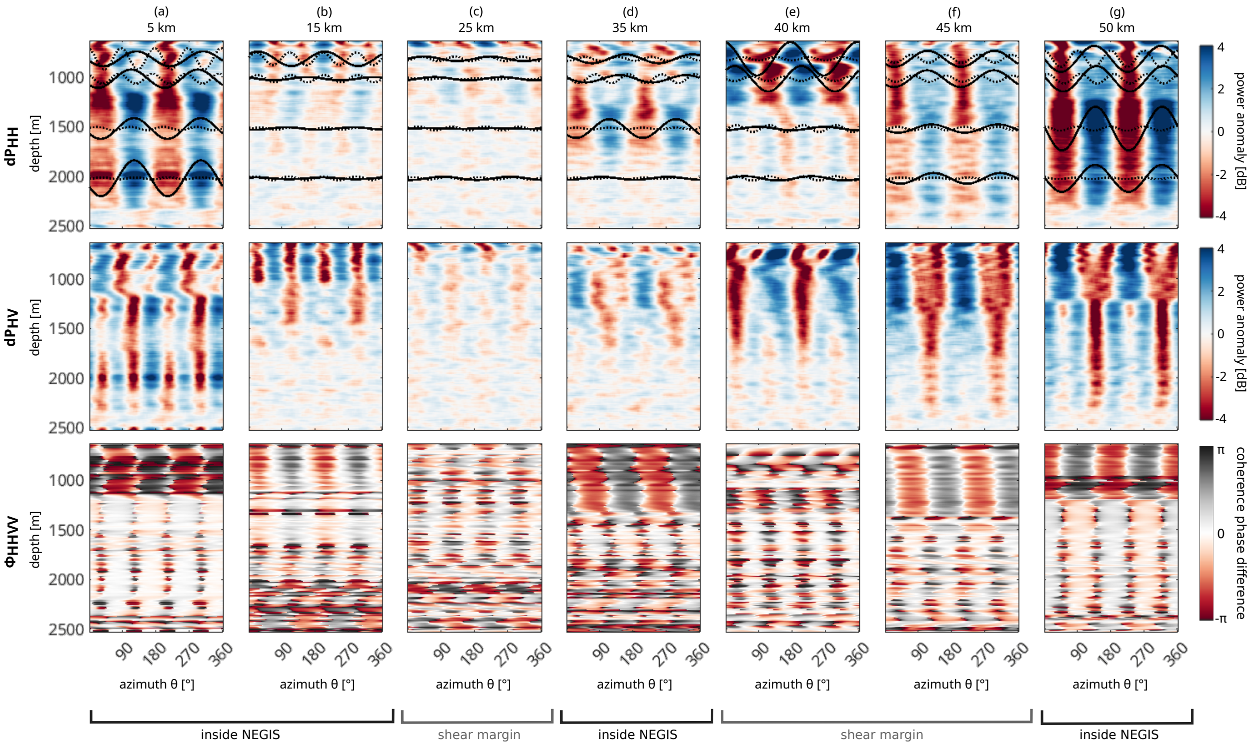


Fig. S8: Synthesized azimuthal radar response for profile '20220706': top panels show the co-polarized power anomaly $dP_{HH}$, middle panels show the cross-polarized power anomaly $dP_{HV}$, and bottom panels show the coherence phase difference $\phi_{HHVV}$.

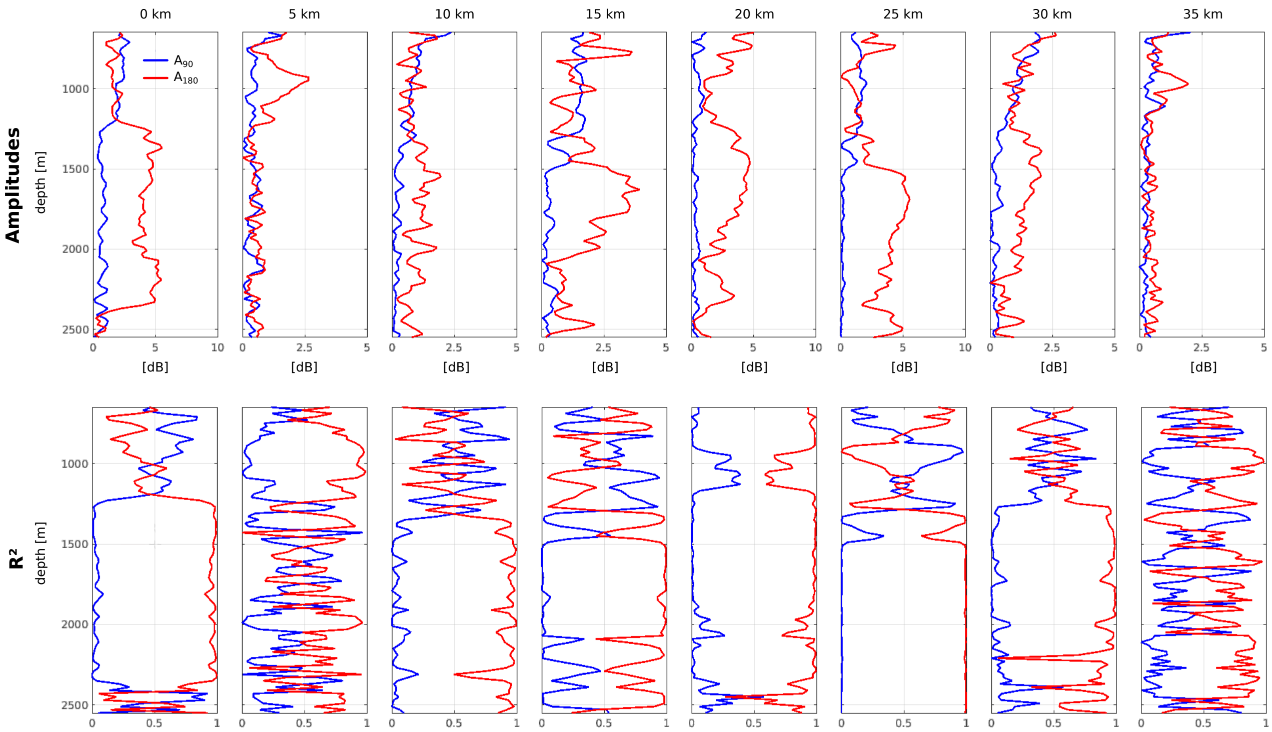


Fig. S9: Amplitudes and goodness of fit for 90°- and 180°-periodic sine curve in profile '20220627'. Top panels show the amplitudes of birefringence (blue) and scattering (red) in dB at 5 km intervals along the profile, with start and driving direction indicated in Fig. S3. Bottom panels show the coefficient of determination ($R^2$), indicating the goodness of the fit, ranging from 0 to 1, for both curves.

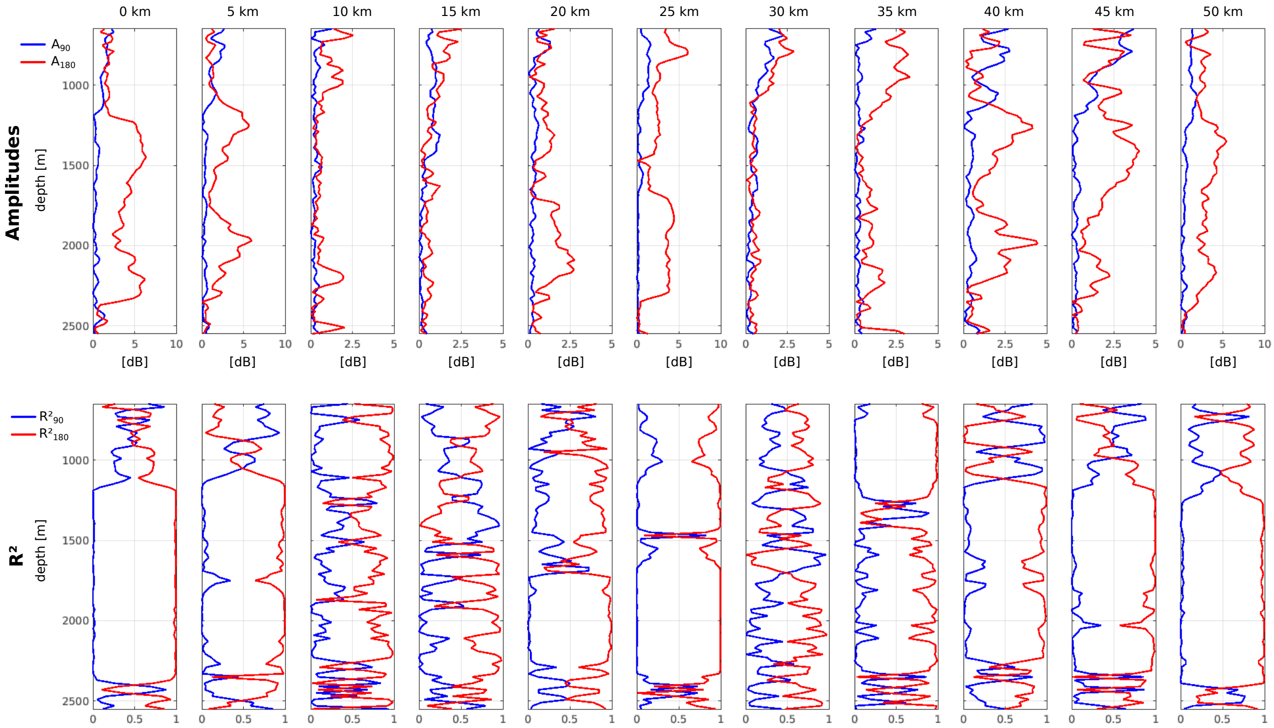


Fig. S10: Amplitudes and goodness of fit for 90°- and 180°-periodic sine curve in profile '20220628'. Top panels show the amplitudes of birefringence (blue) and scattering (red) in dB at 5 km intervals along the profile, with start and driving direction indicated in Fig. S3. Bottom panels show the coefficient of determination ($R^2$), indicating the goodness of the fit, ranging from 0 to 1, for both curves.

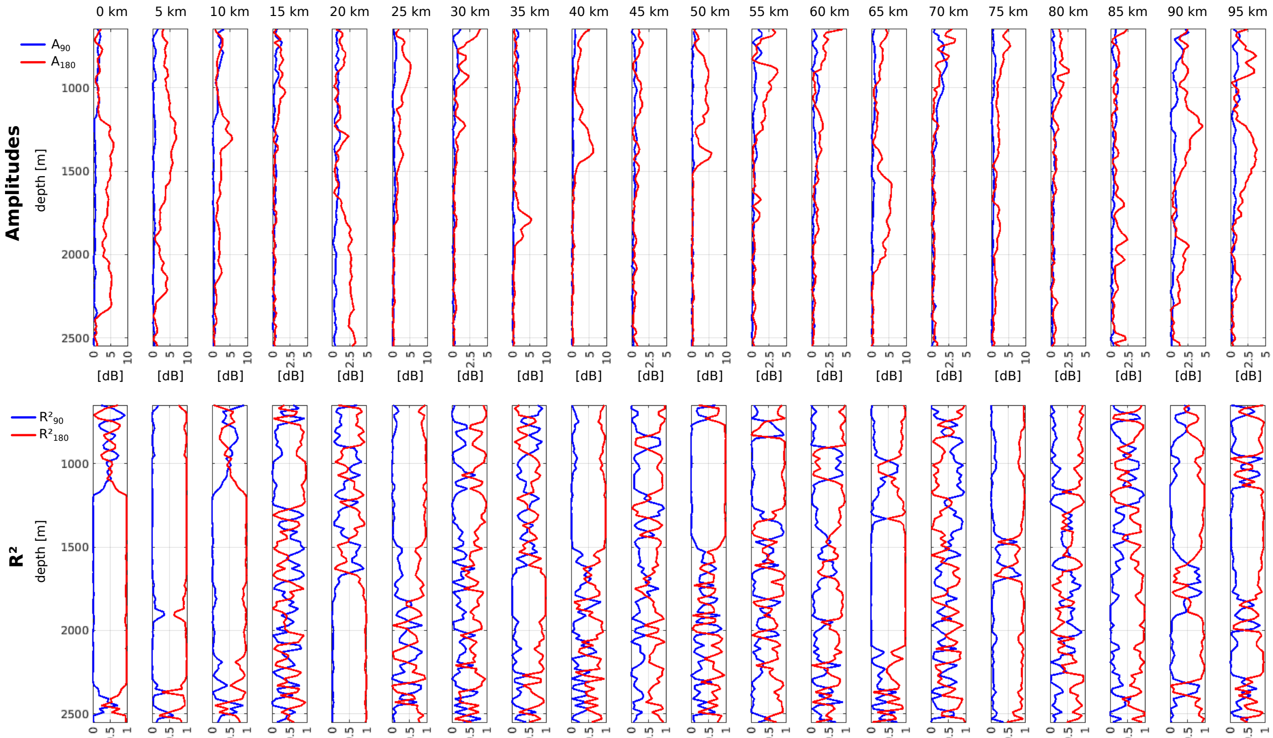

Fig. S11: Amplitudes and goodness of fit for 90°- and 180°-periodic sine curve in profile '20220630'. Top panels show the amplitudes of birefringence (blue) and scattering (red) in dB at 5 km intervals along the profile, with start and driving direction indicated in Fig. S3. Bottom panels show the coefficient of determination ($R^2$), indicating the goodness of the fit, ranging from 0 to 1, for both curves.

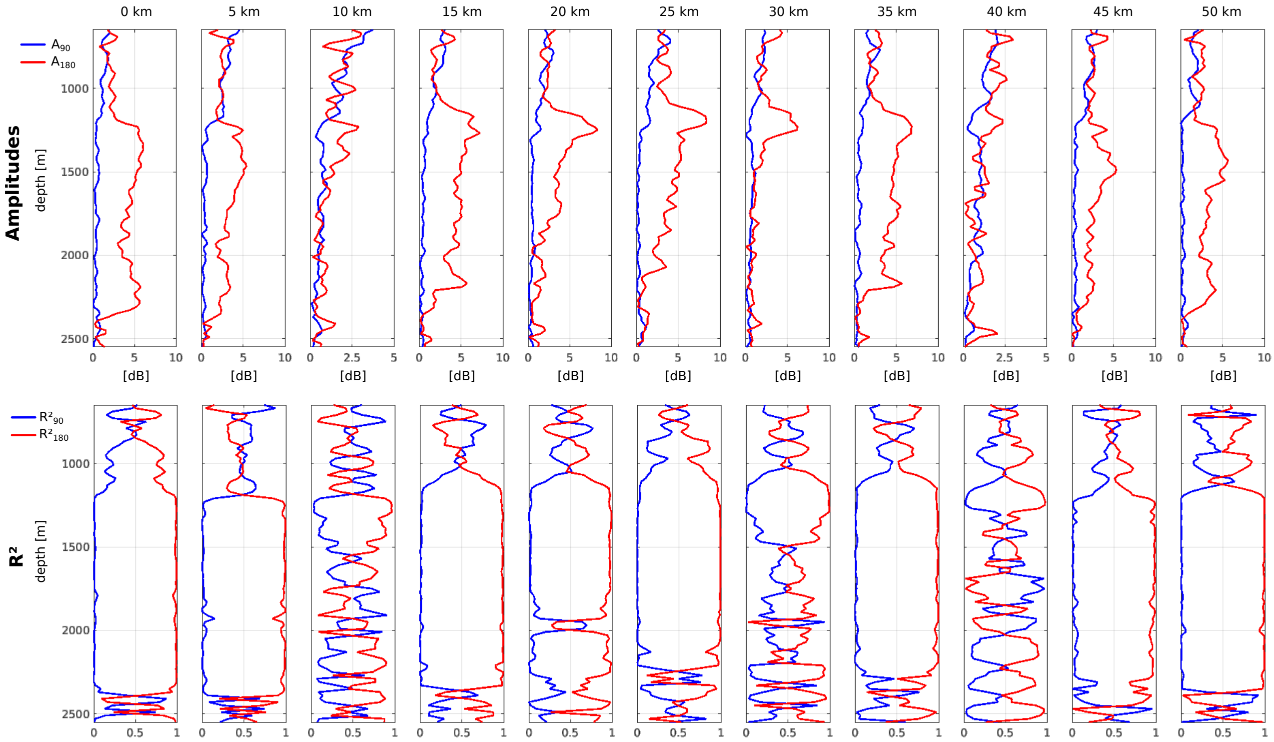


Fig. S12: Amplitudes and goodness of fit for 90°- and 180°-periodic sine curve in profile '20220704'. Top panels show the amplitudes of birefringence (blue) and scattering (red) in dB at 5 km intervals along the profile, with start and driving direction indicated in Fig. S3. Bottom panels show the coefficient of determination ($R^2$), indicating the goodness of the fit, ranging from 0 to 1, for both curves.

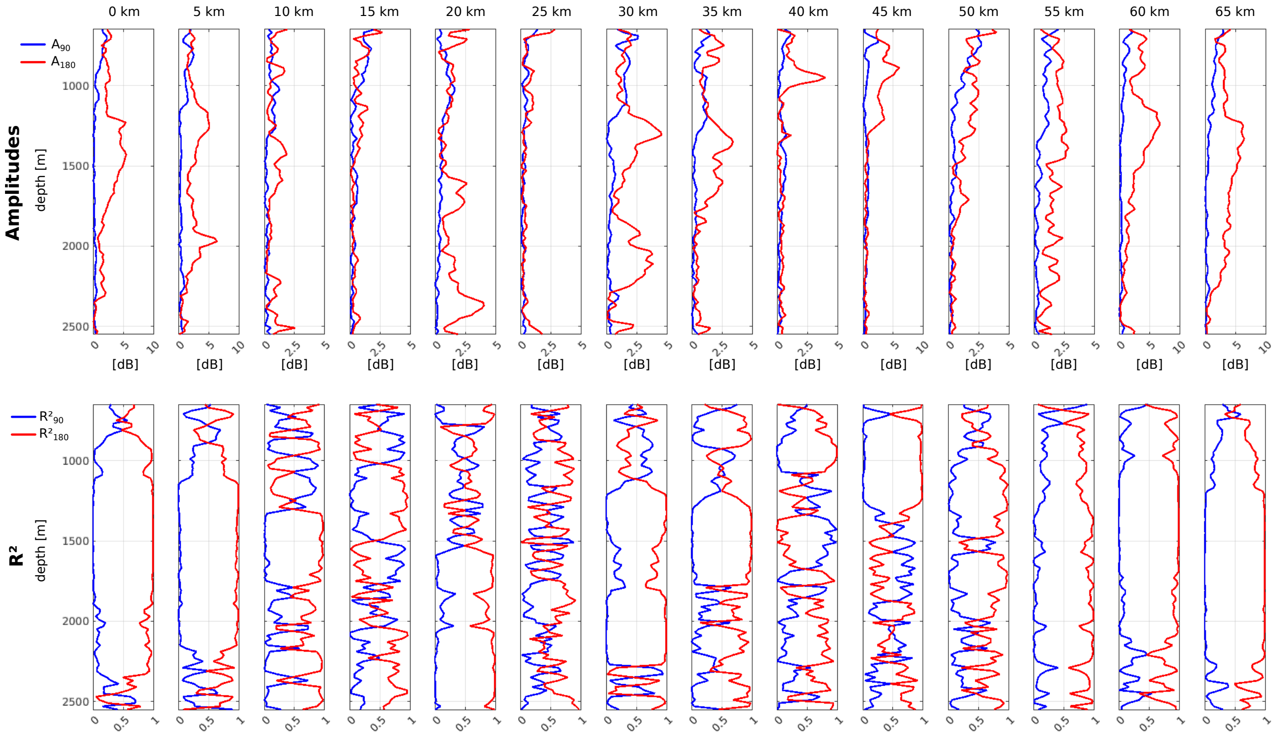


Fig. S13: Amplitudes and goodness of fit for 90°- and 180°-periodic sine curve in profile '20220706'. Top panels show the amplitudes of birefringence (blue) and scattering (red) in dB at 5 km intervals along the profile, with start and driving direction indicated in Fig. S3. Bottom panels show the coefficient of determination ($R^2$), indicating the goodness of the fit, ranging from 0 to 1, for both curves.

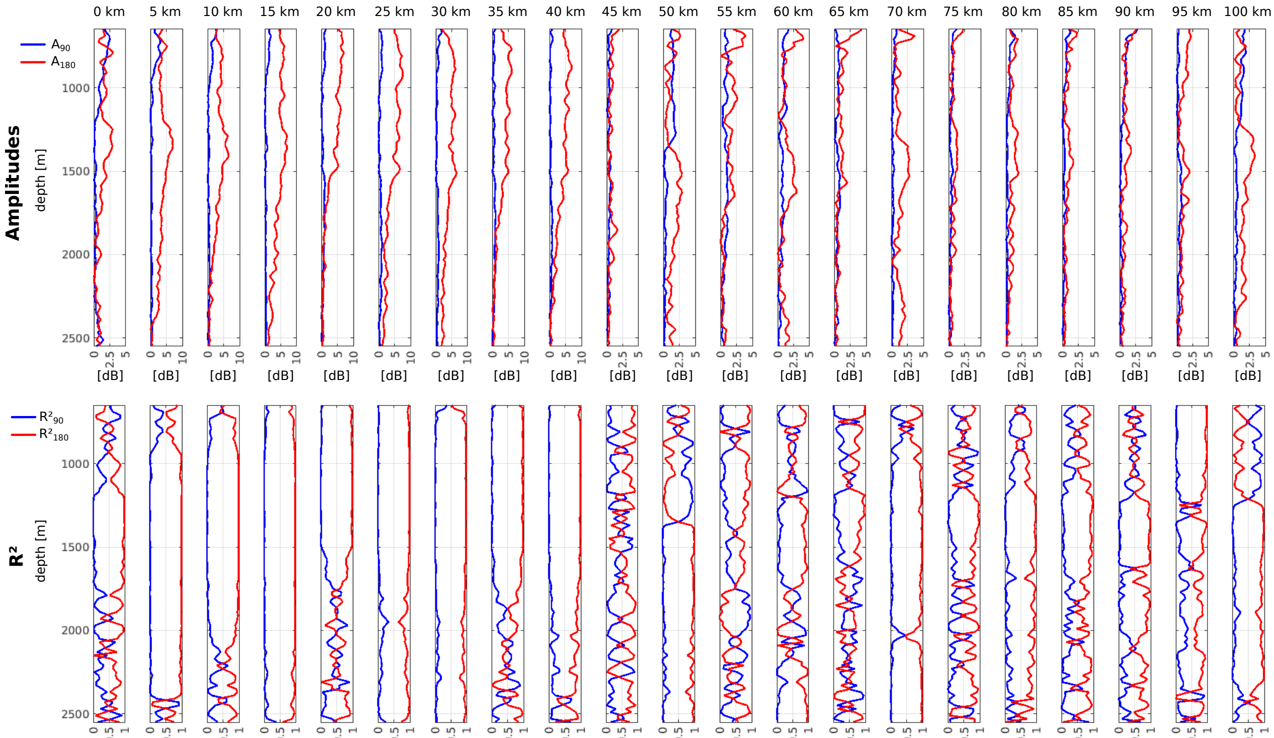


Fig. S14: Amplitudes and goodness of fit for 90°- and 180°-periodic sine curve in profile A (see Fig. 1). Top panels show the amplitudes of birefringence (blue) and scattering (red) in dB at 5 km intervals along the profile, with start and driving direction indicated in Fig. S3. Bottom panels show the coefficient of determination ($R^2$), indicating the goodness of the fit, ranging from 0 to 1, for both curves.

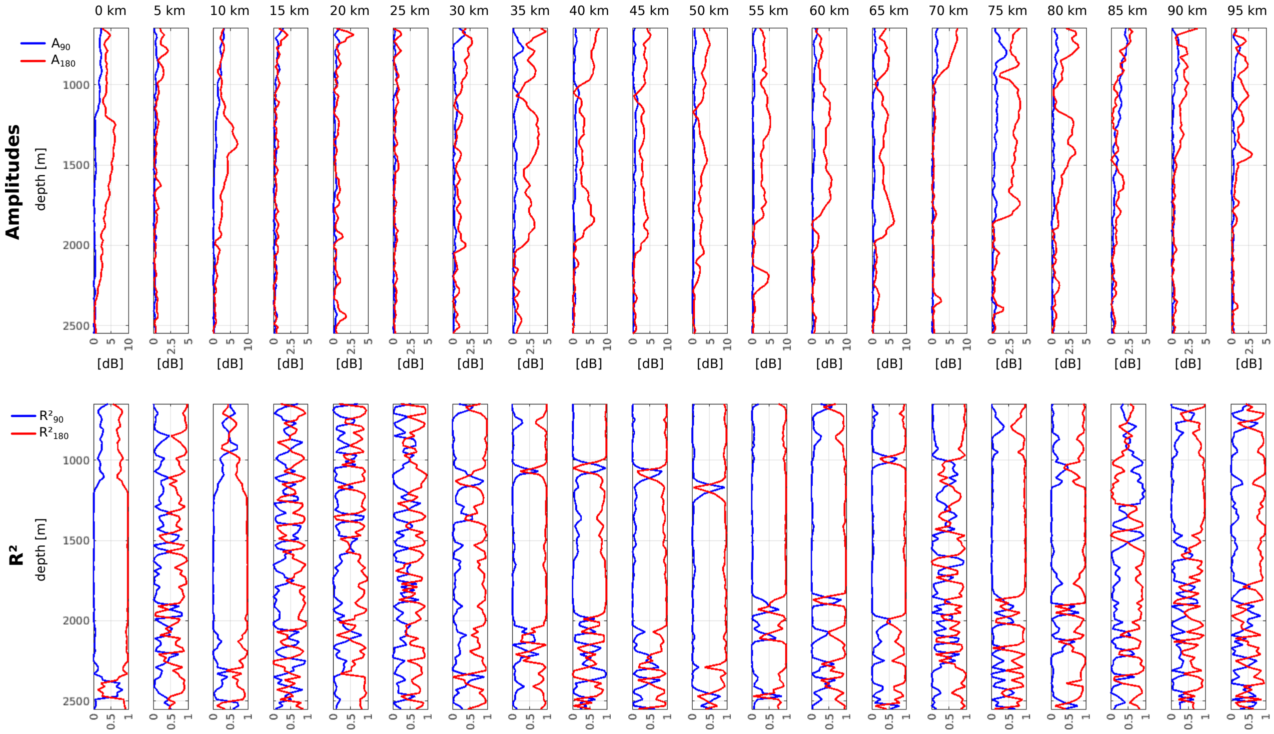


Fig. S15: Amplitudes and goodness of fit for 90°- and 180°-periodic sine curve in profile B (see Fig. 1). Top panels show the amplitudes of birefringence (blue) and scattering (red) in dB at 5 km intervals along the profile, with start and driving direction indicated in Fig. S3. Bottom panels show the coefficient of determination ($R^2$), indicating the goodness of the fit, ranging from 0 to 1, for both curves.

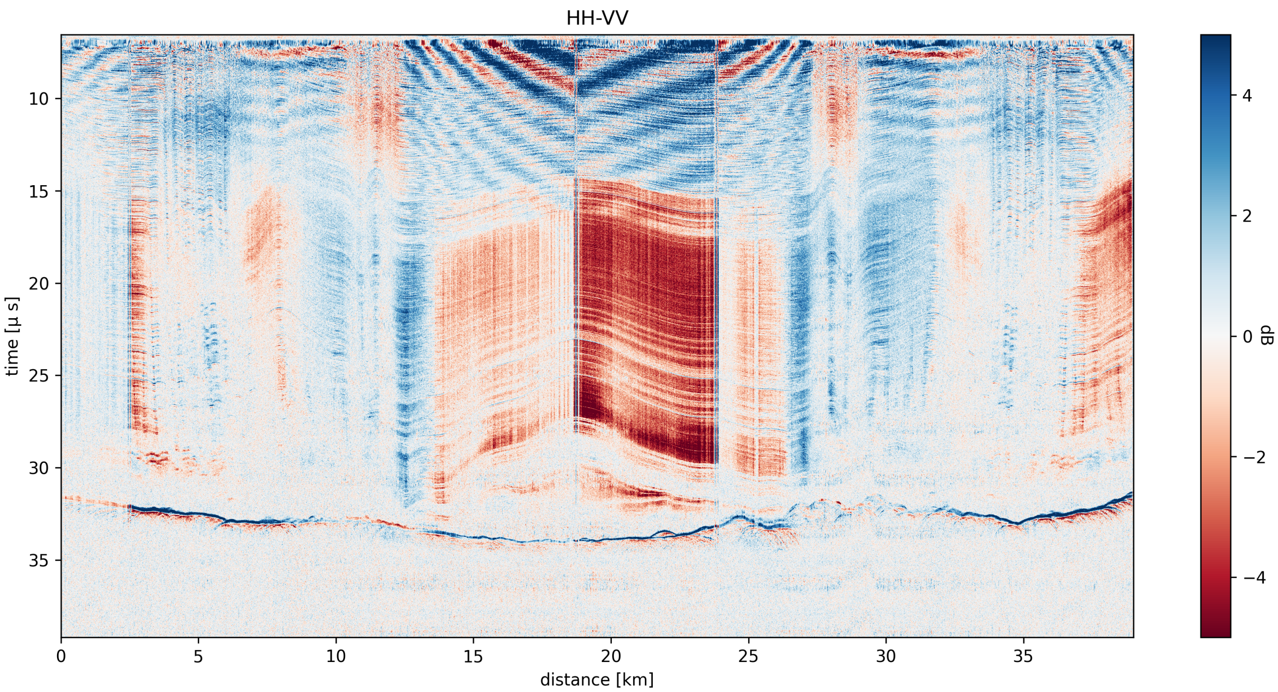


Fig. S16: HH-VV power difference for profile '20220627'.

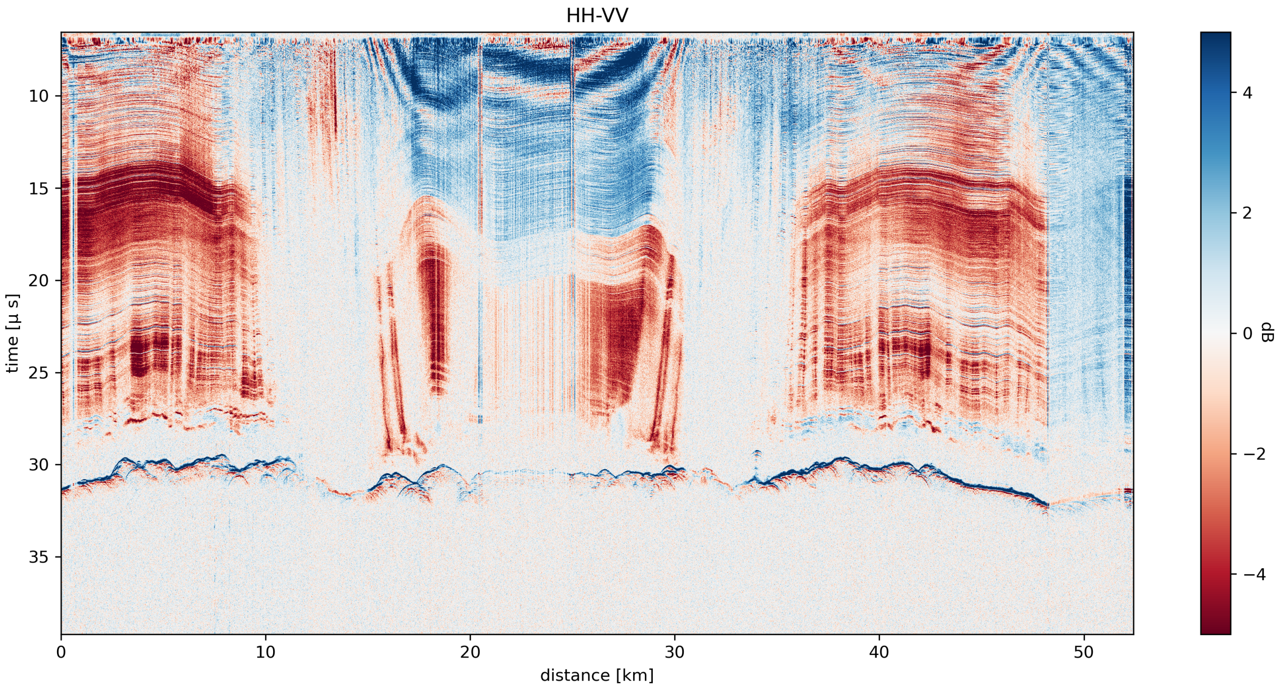


Fig. S17: HH-VV power difference for profile '20220628'.

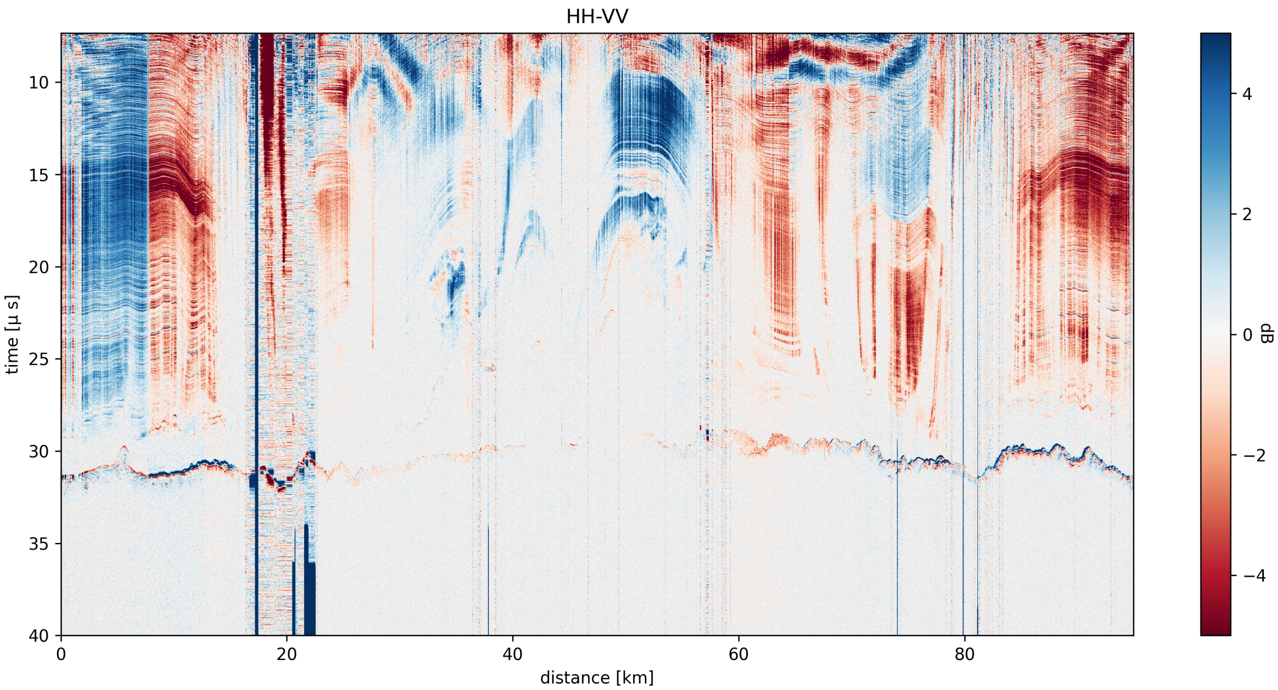


Fig. S18: HH-VV power difference for profile '20220630'.

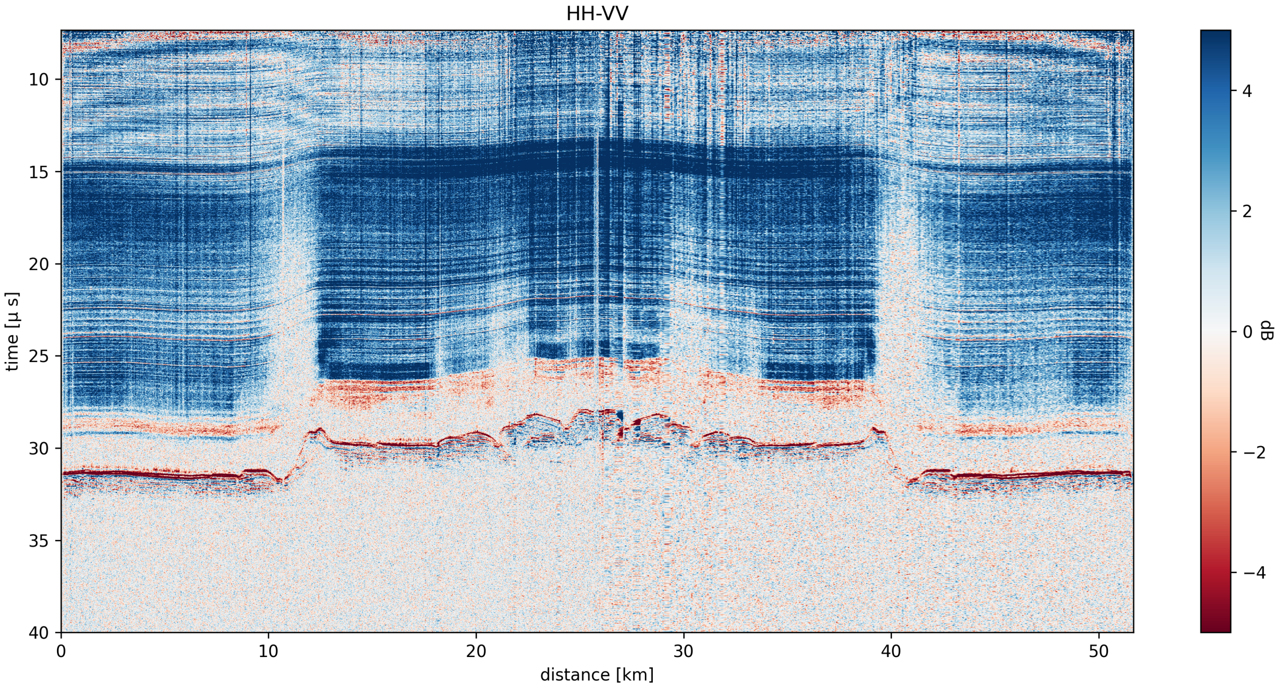


Fig. S19: HH-VV power difference for profile '20220704'.

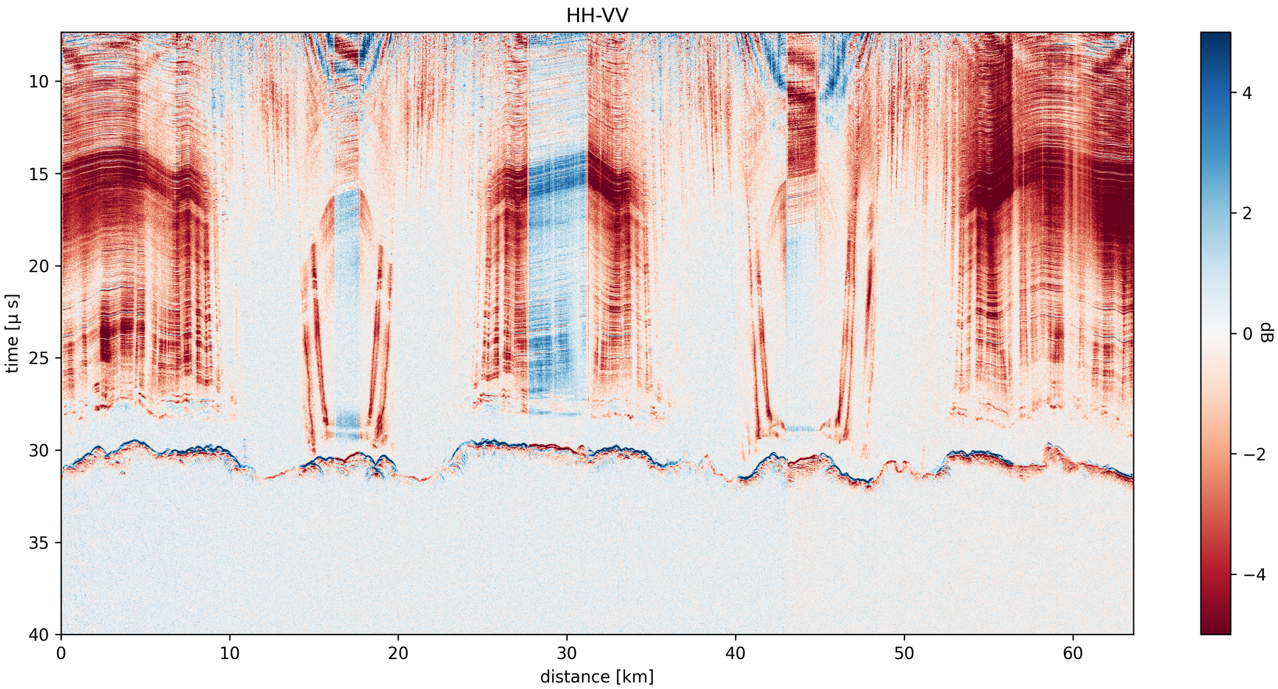


Fig. S20: HH-VV power difference for profile '20220706'.

## References


Dall, J.: Ice sheet anisotropy measured with polarimetric ice sounding radar, IEEE international geoscience and remote sensing symposium, pp. 2507–2510, https://doi.org/10.1109/IGARSS.2010.5653528, 2010.

Ershadi, M. R., Drews, R., Martín, C., Eisen, O., Ritz, C., Corr, H., Christmann, J., Zeising, O., Humbert, A., and Mulvaney, R.: Polarimetric radar reveals the spatial distribution of ice fabric at domes and divides in East Antarctica, The Cryosphere, 16, 1719–1739, https://doi.org/10.5194/tc-16-1719-2022, 2022.

Fujita, S., Matsuoka, T., Ishida, T., Matsuoka, K., and Mae, S.: A summary of the complex dielectric permittivity of ice in the megahertz range and its applications for radar sounding of polar ice sheets, in: Physics of ice core records, pp. 185–212, Hokkaido University Press, 2000.

Fujita, S., Maeno, H., and Matsuoka, K.: Radio-wave depolarization and scattering within ice sheets: a matrix-based model to link radar and ice-core measurements and its application, Journal of Glaciology, 52, 407–424, https://doi.org/10.3189/172756506781828548, 2006.

Jordan, T. M., Schroeder, D. M., Castelletti, D., Li, J., and Dall, J.: A polarimetric coherence method to determine ice crystal orientation fabric from radar sounding: Application to the NEEM ice core region, IEEE Transactions on Geoscience and Remote Sensing, 57, 8641–8657, https://doi.org/10.1109/TGRS.2019.2921980, 2019.

Matsuoka, T., Fujita, S., Morishima, S., and Mae, S.: Precise measurement of dielectric anisotropy in ice Ih at 39 GHz, Journal of Applied Physics, 81, 2344–2348, https://doi.org/10.1063/1.364238, 1997.

Rathmann, N. M., Lilien, D. A., Grinsted, A., Gerber, T. A., Young, T. J., and Dahl-Jensen, D.: On the limitations of using polarimetric radar sounding to infer the crystal orientation fabric of ice masses, Geophysical Research Letters, 49, e2021GL096 244, https://doi.org/10.1029/2021GL096244, 2022.

Westhoff, J., Stoll, N., Franke, S., Weikusat, I., Bons, P., Kerch, J., Jansen, D., Kipfstuhl, S., and Dahl-Jensen, D.: A stratigraphy-based method for reconstructing ice core orientation, Annals of Glaciology, 62, 191–202, https://doi.org/10.1017/aog.2020.76, 2021.

Zeising, O., Gerber, T. A., Eisen, O., Ershadi, M. R., Stoll, N., Weikusat, I., and Humbert, A.: Improved estimation of the bulk ice crystal fabric asymmetry from polarimetric phase co-registration, The Cryosphere, 17, 1097–1105, https://doi.org/10.5194/tc-17-1097-2023, 2023.